ACS OMEGA

http://pubs.acs.org/journal/acsodf

Article

Ex Situ Method for Photoreduction of the Cadmium Ion from Terbium-Loaded Bismuth Vanadium Oxide

Faria K. Naqvi, Kaseed Anwar, and Saba Beg*

Cite This: *ACS Omega* 2021, 6, 31716−31726

Read Online

ACCESS | Metrics & More | Article Recommendations

ABSTRACT: The photoreduction of Cd (II) to Cd (0) was performed using $Bi_4V_2O_{11}$, which was tremendously enhanced by Tb^{3+}-doped $Bi_4V_2O_{11}$. The relationship between charge carrier isolation and light harvesting was studied in depth in this research, and a promising technique for fabricating effective photocatalysts for heavy metals was discovered. Lattice disorder effects due to size variance between V^{5+} and Tb^{3+} cations in $Bi_4V_2O_{11}$ nanomaterials substituted with an invariable Tb^{3+} cation at different concentrations (x = 15, 20, and 25%). $Bi_4V_2O_{11}$ and 15% $Tb/Bi_4V_2O_{11}$ evidenced a coexistence of monoclinic (α-phase) with a *CS/m* symmetry, while 25% $Tb/Bi_4V_2O_{11}$ was tetragonal (γ-phase) with an *I*4/*mmm* symmetry. Raman scattering experiments elucidated the changes in $Bi_4V_2O_{11}$ lattice corresponding to oxygen motion, suggesting significant destabilization of the VO_4 tetrahedra after addition of Tb^{3+}. The SEM micrograph depicted a disparity in the microstructure with reduced grain size in 25% $Tb/Bi_4V_2O_{11}$ samples. However, the TEM micrographs of 25% $Tb/Bi_4V_2O_{11}$ nanomaterials revealed that crystallite sizes of 25−35 nm were obtained, presenting a single tetragonal phase, highly homogeneous in nature. Impedance spectroscopy was used to study the conductivity of these compounds in the temperature range of 300 °C. At 300 °C, the compounds with x = 25% showed a conductivity of 15.92 S cm^{-1}. The conductivity values were found to be comparable with the highest values reported in the literature for similar compounds.

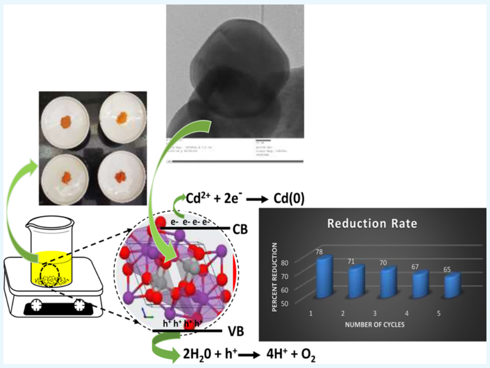

1. INTRODUCTION

Heavy metals such as lead, mercury, cadmium, nickel, and chromium are found in the wastewater of various industries such as mining, petrochemicals, pharmaceuticals, plastic products, paper, and fabric dyeing.[1−4] Because of the adverse effects of heavy metals, many of their derivatives are classified as pollutants.[2] Penetration of heavy metals inside the body leads to various adverse effects and also many diseases.[5] Inclusion of heavy metals' in the marine bodies contributed to pollution and side effects in marine organisms.[6]

Cadmium is toxic for human and animal health, which enters water through agriculture processes and chemical industries such as electroplating, metallurgical alloying, metal finishing, ceramics, cadmium-containing pigments, textile printing, plastic processing, cadmium-containing phosphate fertilizers, refined petroleum oil, and detergents.[6,7] Due to these many adverse effects, the removal of cadmium from the water bodies is essential. Scientists are trying to imply various methods to remove cadmium from contaminated water bodies. To treat the contaminated water bodies, standard treatment procedures such as precipitation, ion exchange, reverse osmosis, and adsorption were used. Environmental and health regulatory agencies have mandated biological processes with low affinity and selectivity for reducing residual cadmium concentrations.[8−12] In addition, Cd is toxic in its 2+ oxidation state and this is the only form which can be captured and reduced to the zero oxidation state which is nontoxic.[12] Cadmium belongs to group 12 in the periodic table and usually prefers to be in the 2+ oxidation state. The Cd^{2+} ion has capability to combine with almost every element (such as oxide, sulfide, nitrite, etc.). These elements are almost impossible to remove from water bodies. However, when cadmium is in the zero state, it acts as a noncorrosive element.[8,13,14] As a result, developing a new approach for converting toxic Cd (II) to nontoxic Cd (0) is essential. The reduction of heavy metals using photocatalytic methods is a safe, green, and low-cost purification technique for the metal ion treatment procedure. Pollutants were immediately reduced to the metallic state in this method, rendering this property under the section of green chemistry.[11,12,15]

Recently, bismuth vanadium oxide ($Bi_4V_2O_{11}$) has emerged as a semiconductor since it generates electron−hole pairs.

Received: August 14, 2021
Accepted: November 1, 2021
Published: November 16, 2021

https://doi.org/10.1021/acsomega.1c04400
ACS Omega 2021, 6, 31716−31726

Metal ions absorb photogenerated electrons from the semiconductor conduction band (CB) and are reduced into a nontoxic state. Photoreduction has been thoroughly researched to eliminate many heavy metals, including lead, chromium, nickel, cadmium, and mercury, during the past decade. There are several reports on semiconductor photocatalysts under UV light for cadmium ion reduction.[16,17] The Cd (II) photoreduction process requires three different quenching agents, isopropanol (IPA, 10 mM, $^{\bullet}$OH quencher), potassium iodide (KI, 10 mM, h^+ and $^{\bullet}$OH quencher), and benzoquinone (BQ, 1 Mm, $^{\bullet}O_2^-$ quencher). Hole scavengers primarily inhibit charge carrier recombination.[15,18−20] They also generate secondary reducing hydroxyl radicals, which help with photoreduction.[18,21] The choice of an effective photocatalyst is critical in this photoreduction process. Bismuth vanadium oxide ($Bi_4V_2O_{11}$) and doped $Bi_4V_2O_{11}$ possess some unique properties such as low band gap, low cost, high stability, availability, and environmental friendly nature, which make it an ultimate choice as a catalyst.[3,22] The photoreduction efficiency strongly depends on the catalyst physical features such as band gaps.[2,23] Therefore, for improving the recombination rate of photogenerated electrons and holes in $Bi_4V_2O_{11}$, modification of its activity in the UV−visible region, is necessary.[10,12,15,16,18] Tb^{3+} as a low-band-gap material and UV−vis-driven agent has attracted interest because of its low toxicity. Therefore, in this research, it has been attempted to reduce cadmium ions using a Tb^{3+}-doped $Bi_4V_2O_{11}$ ($Tb/Bi_4V_2O_{11}$) photocatalytic system to boost the adsorption and reduction performance. $Tb/Bi_4V_2O_{11}$ is also known for its oxide ion conductivity at an intermediate temperature. $Bi_4V_2O_{11}$ is built from $(Bi_2O_2)^{2+}$ layers separated by $(A_{n-1}B_nO3_{n+1})^{2-}$ perovskite-like slabs, where n = 1, 2, 3, ... 8, which represents the thickness of the perovskite layers in terms of BO_6 octahedra.[24−27] They are stabilized in three polymorphic forms α, β, and γ as a result of doping at the vanadium site. These polymorphs are interconvertible. From the literature review, we have seen that many d-block and p-block metals which have been introduced at the vanadium site showed good oxide ionic conductivity.[28]

In this study, we synthesized terbium-doped bismuth vanadium oxide ($Tb/Bi_4V_2O_{11}$) nanoparticles via a sol−gel method. It is a convenient way to manufacture non-agglomerated particles having almost equal crystalline size. The size of a particle plays an important role in conduction properties.[29] This method also helps to reduce the sintering temperature.

2. RESULTS AND DISCUSSION

2.1. Crystallographic Studies. Figure 1 shows the XRD patterns of $Bi_4V_2O_{11}$ and $Tb/Bi_4V_2O_{11}$ in the composition range Tb = 15, 20, and 25%. The XRD pattern illustrates the stabilization of the monoclinic (α) phase of $Bi_4V_2O_{11}$, which was confirmed by JCPDS number 82-1481 with a space group symmetry CS/m. The XRD pattern of $Bi_4V_2O_{11}$ and 15% $Tb/Bi_4V_2O_{11}$ shows a characteristic peak at $2\theta = 30.5$ ascribed to (200), which confirms the monoclinic (α) phase. The doublet in $Bi_4V_2O_{11}$ and 15% $Tb/Bi_4V_2O_{11}$ peak at $2\theta = 35°$ ascribed to (220) and (026), respectively, merged to one singlet peak (022) in 20% $Tb/Bi_4V_2O_{11}$, which shows the transformation of the α phase to the orthorhombic (β) phase. β phase transformation is confirmed by JCPDS number 89-4498. The tetragonal (γ) phase is confirmed (JCPDS number 89-0102) for the sample 25% $Tb/Bi_4V_2O_{11}$ at room temperature with a space group symmetry $I4/mmm$. The structure could be distorted by varying doping quantities of Tb^{3+}. The sharpness of (103) peaks at $2\theta = 28.8°$ increases with increase in the dopant concentration. This increment is because of the replacement of the larger-size cation Tb^{3+} (1.18 A°) in the place of the smaller cation vanadium (V^{5+} = 0.54 A°). As a result, the parent compound structure is disrupted and a more stable phase is adapted.[3,30−36]

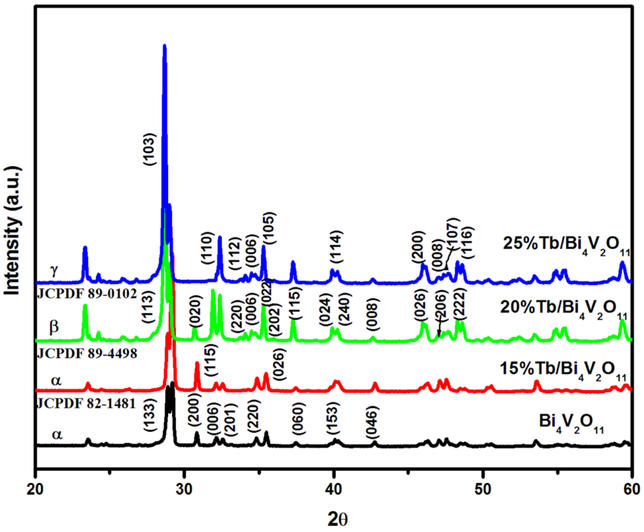

Figure 1. PXRD patterns of terbium-doped bismuth vanadate nanoparticles ($Tb/Bi_4V_2O_{11}$) and parent compound ($Bi_4V_2O_{11}$).

The unit cell parameters of $Tb/Bi_4V_2O_{11}$ are shown in Table 1. The volume decreases with increasing Tb^{3+} content (Table 1) from 15 to 25%. The decrease of lattice parameters might be attributed to the incorporation of Tb^{3+} ions into the $Bi_4V_2O_{11}$ lattice to replace V^{5+} ions. The diffraction peak is also broadened by an increase in the amount of Tb^{3+} doping, suggesting that the crystal size decreased gradually with the increase in the full-width half maximum (fwhm). The average particle size of synthesized nanoparticles can be calculated by the Debye Scherer formula.

Table 1. Unit Cell Parameters for $Bi_4V_2O_{11}$ Are Shown Below

composition	a (Å)	b (Å)	c (Å)	V (Å^3)	phase
$Bi_4V_2O_{11}$	5.612	15.28	16.601	1423.85	α
15% $Tb/Bi_4V_2O_{11}$	5.617	15.29	16.611	1426.61	α
20% $Tb/Bi_4V_2O_{11}$	5.462	5.469	15.867	473.97	β
25% $Tb/Bi_4V_2O_{11}$	3.926		15.449	238.18	γ

$$L_{hkl} = \frac{0.94\lambda}{\beta \cos \theta} \tag{1}$$

where $L_{(hkl)}$ is the average crystallite size, λ is the wavelength, β is the fwhm, and θ is the diffraction angle. The size of the nanoparticles is found to be in between 25 and 35 nm.

2.2. X-ray Photoelectron Spectroscopy. X-ray photoelectron spectroscopy (XPS) uses X-rays of characteristic energy to excite electrons from the atoms. The electrons emitted from the sample are captured, and their intensity is plotted as a function of kinetic energy. In $Tb/Bi_4V_2O_{11}$, this technique is prominently used to find out the oxidation state of the substituted species and oxygen vacancy concentration.[37,38]

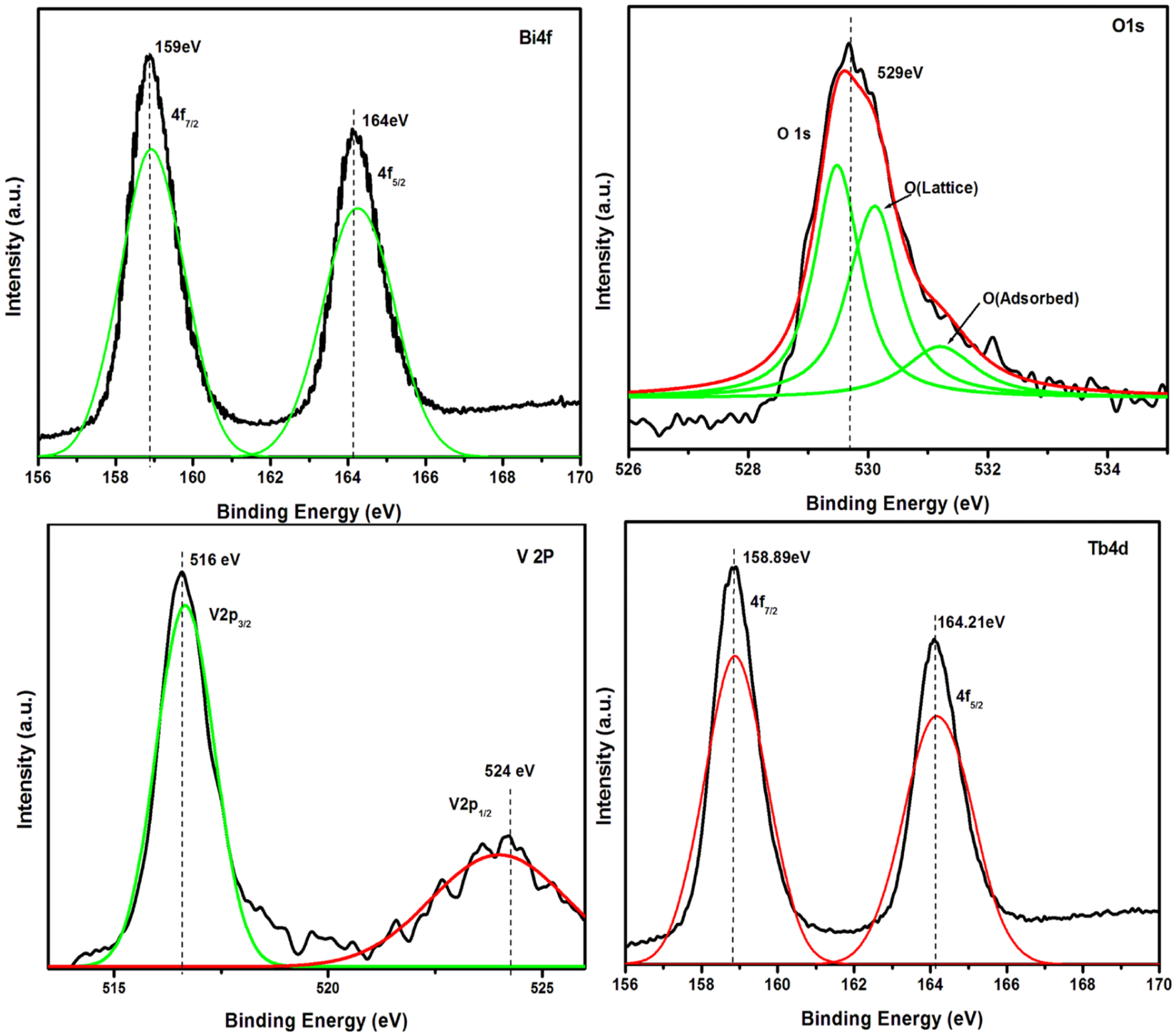

Figure 2. XPS spectra of 25% Tb/$Bi_4V_2O_{11}$: Bi 4f, O 1s, V 2p, and Tb 4d.

The XPS spectra of 25% Tb/$Bi_4V_2O_{11}$ were obtained to classify the valence state of Tb^{3+} (Figure 2). Tb $4d_{5/2}$, Tb $4d_{3/2}$, O 1s, Bi $4f_{7/2}$, Bi $4f_{5/2}$, and C 1s (introduced by CO_2 in air absorbed on the substrate) were in good accordance with the EDX spectra. The binding energies of Bi $4f_{5/2}$ and Bi $4f_{7/2}$, located at 164 and 159 eV, respectively, were observed (Figure 2). Likewise, at 529 eV, the peak of O 1s is present. The vacancies with positive charge on the surface tend to adsorb some negatively charged species, such as OH^- and O^{2-}, whose binding energies are around 531.5 eV, as shown in Figure 2. The peaks of adsorbed O ($O_{adsorbed}$) and lattice O ($O_{lattice}$) on the surface of 25% Tb/$Bi_4V_2O_{11}$ are clearly seen, which is the evidence for vacancy creation in the lattice and responsible for oxygen ion conductivity and catalysis.[39,40] For comparison, the V $2p_{1/2}$ and V $2p_{3/2}$ states for 25% Tb/$Bi_4V_2O_{11}$ at 524 and 516 eV are given. The Tb 4d area (Figure 2d) is shown with distinguishing peaks at 164.21 and 158.89 eV, attributed to Tb $4d_{5/2}$ and Tb $4d_{3/2}$, respectively. The above findings support the inference that in $Bi_4V_2O_{11}$, Tb^{3+} ions replace V^{5+} ions, and this replacement creates oxygen ion vacancies responsible for charge carriers.[41,42]

2.3. Microstructural and Energy-Dispersive Analysis.

Micrographs (Figure 3) show dense nanoparticles with high mechanical stability and good densification. The structure and density of nanomaterials plays an important role in conduction and catalytic properties.[33,43] The micrographs show the presence of agglomerated homogeneous nanoparticles. The particle size is found to be between 25 and 35 nm, analyzed by the software Image J. This is in excellent agreement with the XRD results. Figure 4 shows the microstructures for the samples. In the HRTEM image (Figure 4), a vibrant lattice fringe spacing for $Bi_4V_2O_{11}$ and 25% Tb/$Bi_4V_2O_{11}$ was observed. The lattice distance (d) is about 0.311 nm and 0.312 nm for $Bi_4V_2O_{11}$ and 25% Tb/$Bi_4V_2O_{11}$, respectively. The lattice distances (d) 0.311 nm and 0.312 nm are attributed to (133) and (103), respectively. The SAED pattern Figure 4 clearly shows the small discrete spots making up rings arising from the Bragg reflection, resulting from different spot lineup and forms the ring observed in the HRTEM image.

2.4. Brunauer–Emmett–Teller Measurements.

The isotherms of Tb/$Bi_4V_2O_{11}$ samples of nitrogen adsorption/desorption are presented in Figure 5, indicating the distribution of pores. The sample shows an isotherm of type II, which represents mesoporous powder, a feature of an effective water-degrading photocatalyst. The type II isotherm is the most common one; the flattened region shows the formation of the monolayer. At medium pressure, multilayers will be formed. The synthesis process relies on physicochem-

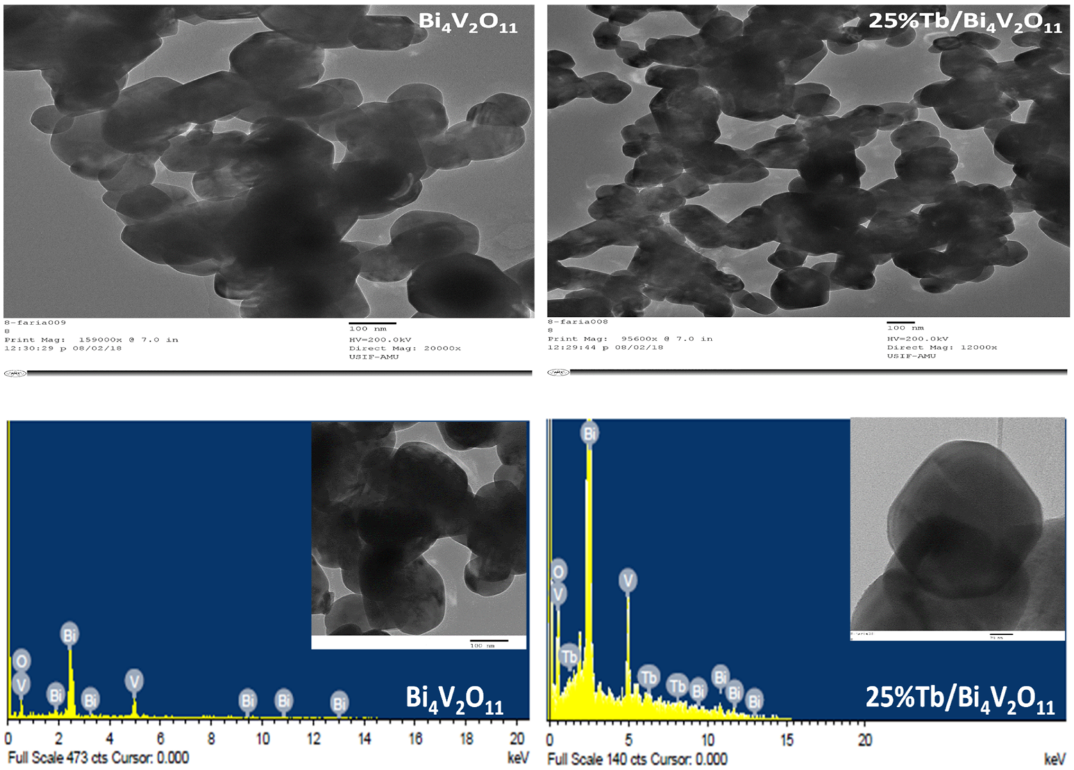

Figure 3. SEM micrographs of $Bi_4V_2O_{11}$ and 25% Tb/$Bi_4V_2O_{11}$ along with their EDX spectra.

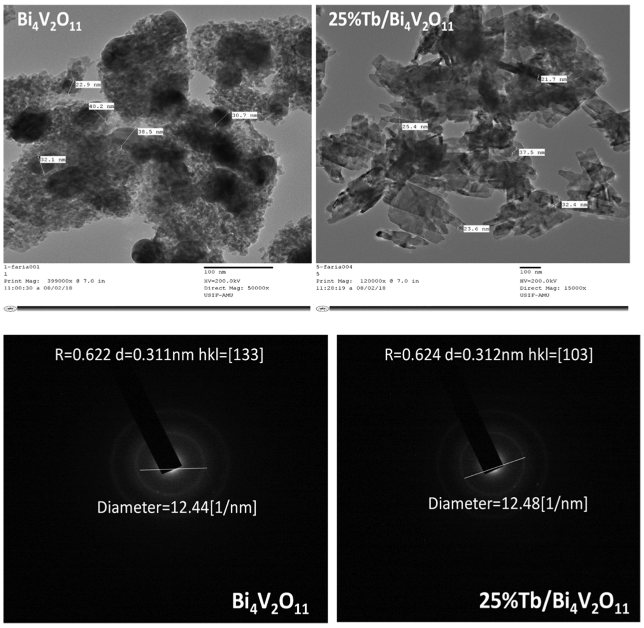

Figure 4. HR-TEM images of $Bi_4V_2O_{11}$ and 25% Tb/$Bi_4V_2O_{11}$ with particle scaling along with the SAED pattern of nanoparticles with *d*-spacing.

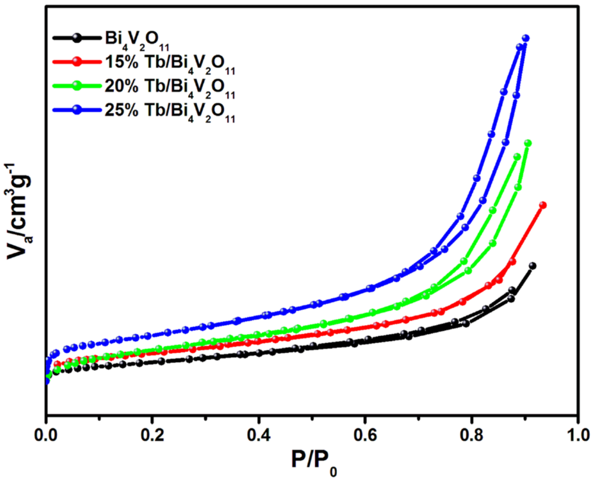

Figure 5. Nitrogen adsorption−desorption isotherms of Tb/$Bi_4V_2O_{11}$.

ical properties including particle size and surface area.[44−47] The adsorption capacity typically varies according to the material surface area; the measured surface area by the BET procedure shows that the adsorption is approximately 47 m^2/g (Figure 5) for 0.25% Tb/$Bi_4V_2O_{11}$. Furthermore, in 25% Tb/$Bi_4V_2O_{11}$ nanoparticles, the increased surface area provides impressive catalytic activity.

2.5. Raman Spectroscopy and Thermogravimetric Analysis.

Raman spectroscopy (Figure 6) is an efficient method for the study of vibrational characteristics in the structure and bonding investigations of metal oxides. $Bi_4V_2O_{11}$ shows the monoclinic phase, in agreement with the XRD and DTA/TGA results (Figure 6b). Monoclinic $Bi_4V_2O_{11}$ shows five clear vibrational peaks at 826, 708, 367, 328, and 208 cm^{-1}. These bands are related to vibrational features of the VO_4 tetrahedron.[48,49] The most intense band is seen at 826 cm^{-1}, which is attributed to the shorter symmetric V−O stretching mode (A_g). The weak band at 708 cm^{-1} was assigned to the short (B_g) asymmetric V−O stretching mode.[50] After doping with terbium (x = 15, 20, and 25%), the V−O stretching mode shifted toward a lower wavenumber (826−

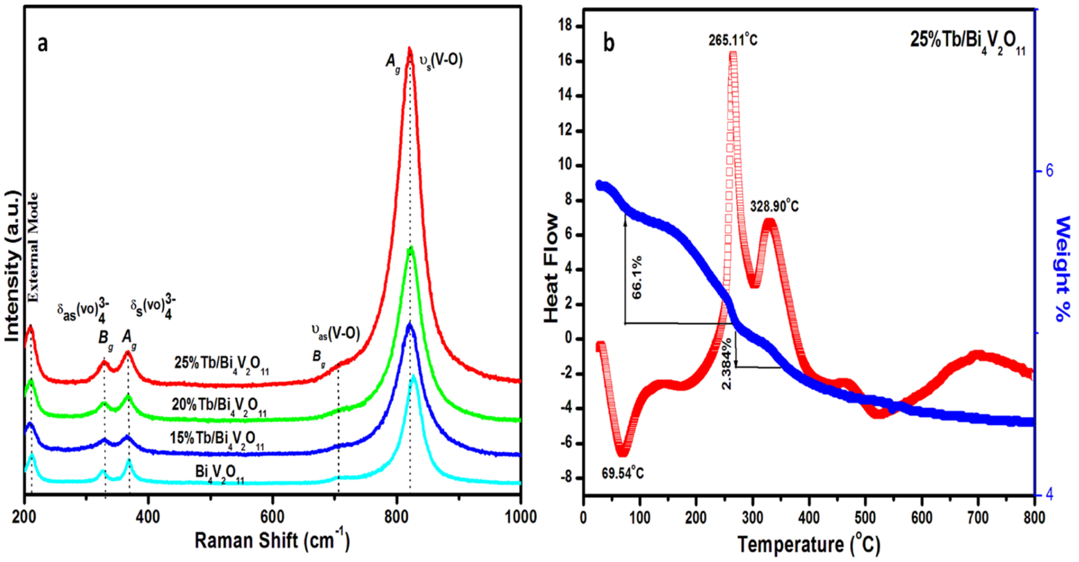

Figure 6. (a) Raman spectra of Tb/$Bi_2V_4O_{11}$ samples with assignments of stretching and bending modes. (b) TG/DTA of 25% Tb/$Bi_2V_4O_{11}$ showing the stability of the nanomaterial.

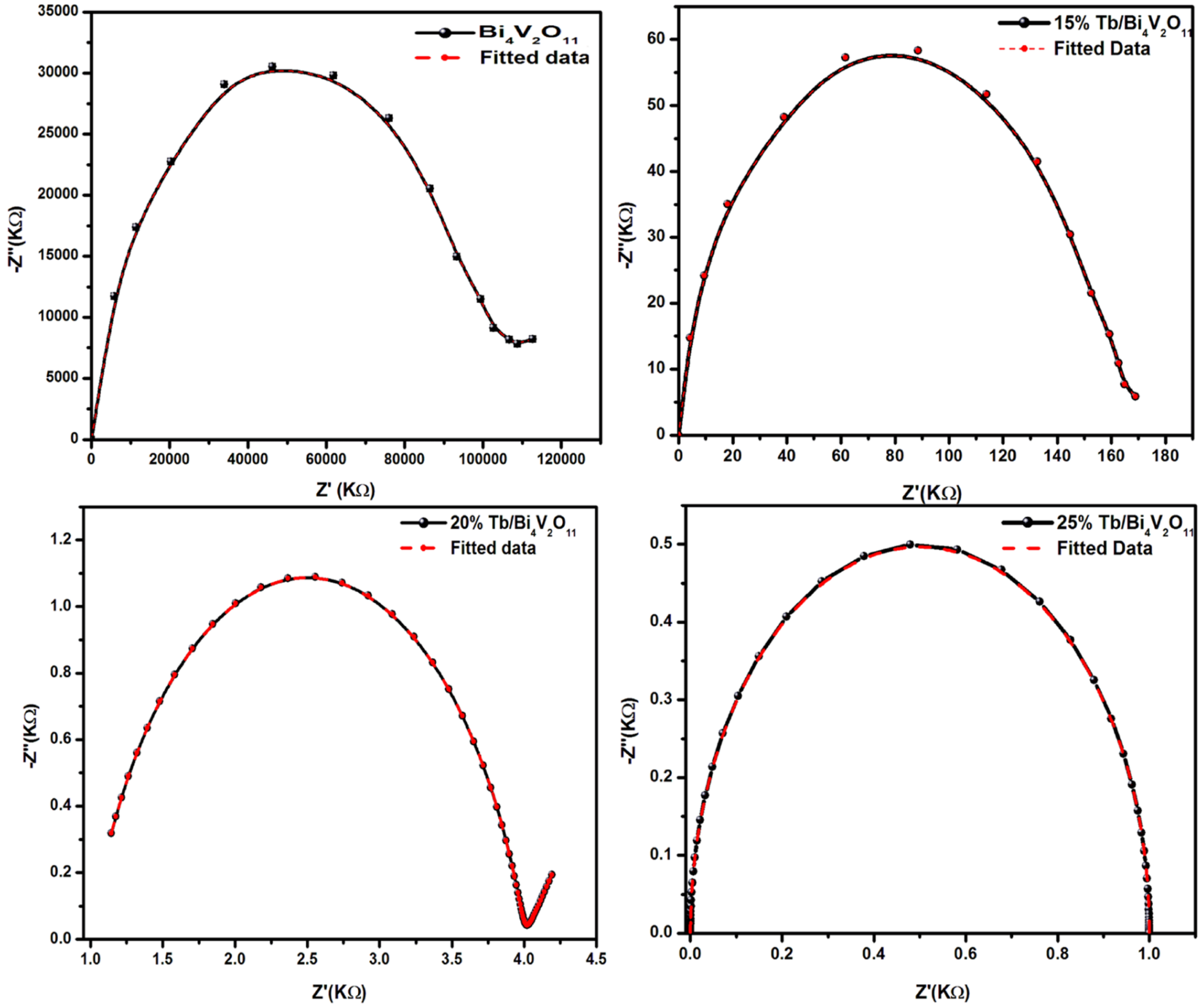

Figure 7. Nyquist plots for different concentrations of Tb/$Bi_4V_2O_{11}$ (15, 20, and 25%) and the parent compound ($Bi_4V_2O_{11}$).

819 cm^{-1}) as compared to $Bi_4V_2O_{11}$. This maybe because of the elongation of the V−O bond length due to the incorporation of Tb^{3+} (ionic radii approx. 1.18 Å) larger cations in the place of V^{5+} (ionic radius approx. 0.54 Å) smaller cations. The fwhm of the peak at 826 cm^{-1} with the symmetric stretching mode increased as the Tb^{3+} concentration increased.

Table 2. Equivalent Circuit Parameters Estimated from the Nyquist Plots for Different Compositions of $Bi_4V_2O_{11}$

composition x	R_1	R_2	R_g	$f_{max,g}$	ω_g	Cg	ζ_g	conductivity σ_{300}
$Bi_4V_2O_{11}$	00	10,231	10,231	56,170	3.53×10^5	2.83×10^{-7}	4.69×10^{-6}	1.56×10^{-3}
15% $Tb/Bi_4V_2O_{11}$	00	165	165.00	30,310	1.90×10^5	3.18×10^{-8}	5.24×10^{-6}	9.65×10^{-2}
20% $Tb/Bi_4V_2O_{11}$	1.12	4.04	005.16	10,000	6.28×10^6	3.43×10^{-7}	1.59×10^{-5}	3.086
25% $Tb/Bi_4V_2O_{11}$	00	1	1	10,471	6.58×10^4	1.52×10^{-5}	6.5×10^{-4}	15.92

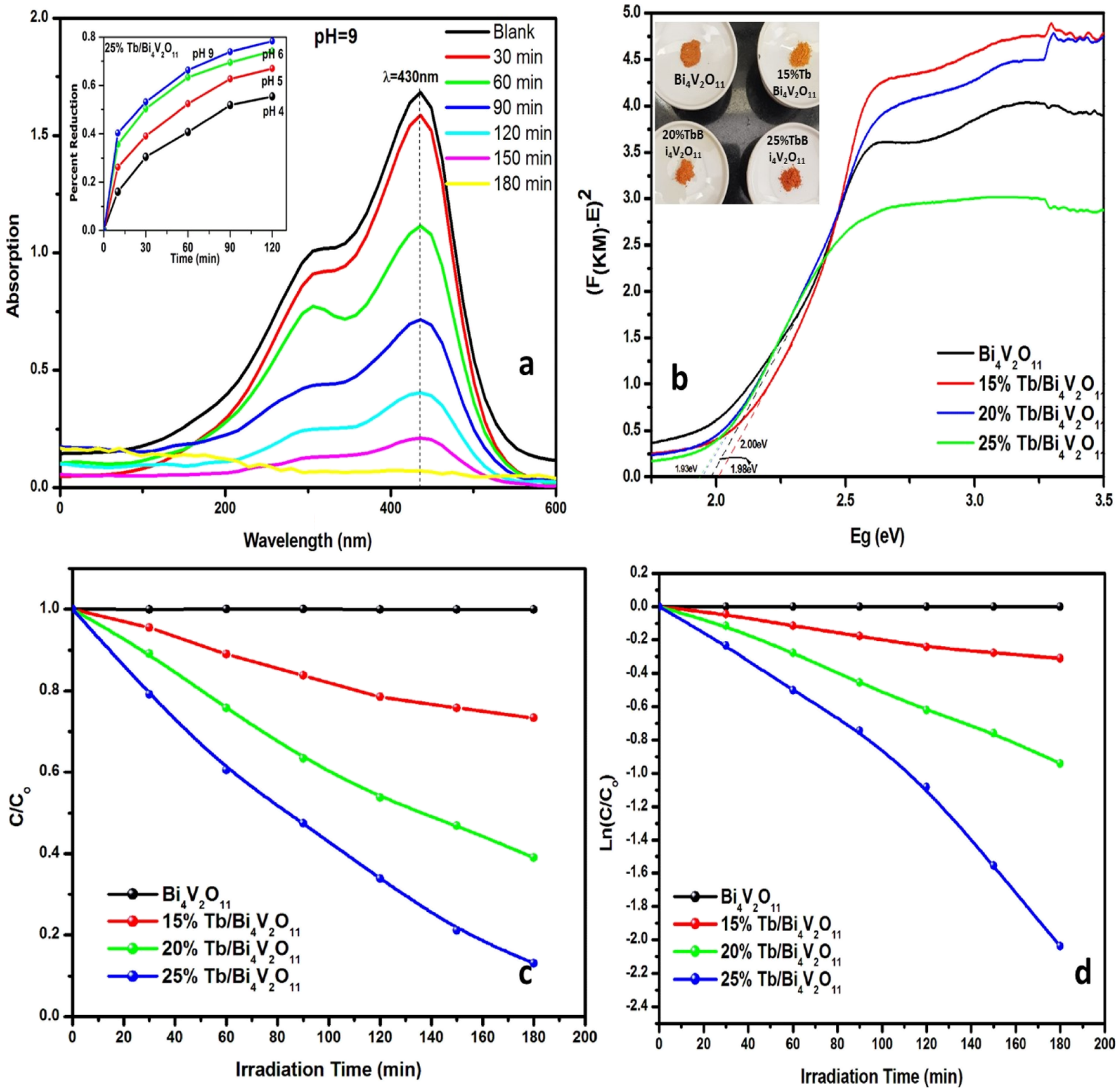

Figure 8. (a) Change in absorbance upon irradiation of cadmium (Cd) (λ_{max} = 430 nm) in the presence of 25% $Tb/Bi_4V_2O_{11}$, (b) Tauc plot for band gap calculation of the synthesized nanomaterials (shown in the inset "Photograph courtesy of Faria K. Naqvi,. Copyright 2021"), (c) change in the concentration of Cd as a function of irradiation time, and (d) kinetic fit for the reduction of Cd (II) in the presence of $Bi_4V_2O_{11}$ and 10% $Tb/Bi_4V_2O_{11}$, 15% $Tb/Bi_4V_2O_{11}$, and 25% $Tb/Bi_4V_2O_{11}$ under visible-light illumination.

This behavior corresponds to the degree of defects including oxygen vacancies.[51] This conclusion is in good agreement with the results of XRD.

2.6. AC Impedance Studies. The electrical conductivity measurements for $Bi_4V_2O_{11}$ and $Tb/Bi_4V_2O_{11}$ nanoparticles of composition x = 0.0, 15, 20, and 25% in the temperature range from 100 to 600 °C using AC impedance spectroscopy were done. The results of AC impedance spectroscopy measurements carried out for different compositions at 300 °C are shown in the Nyquist plot (Figure 7).[52−54] Here, the depressed arcs that correspond to the grain and grain boundary conductivities are highly overlapped due to the similar relaxation times of the charge carriers inside the grain and the grain boundaries.[55,56] The total resistance (R_t) is the sum of these two resistances. The impedance spectra clearly exhibit that both the grain and grain boundary resistances decrease with increasing temperature and the composition. 25% $Tb/Bi_4V_2O_{11}$ shows the lowest resistance value. The equivalent circuit shown in Figure 7 in series with electrolyte resistance was used for the analysis of the impedance spectra and the assessment of the grain element contribution.

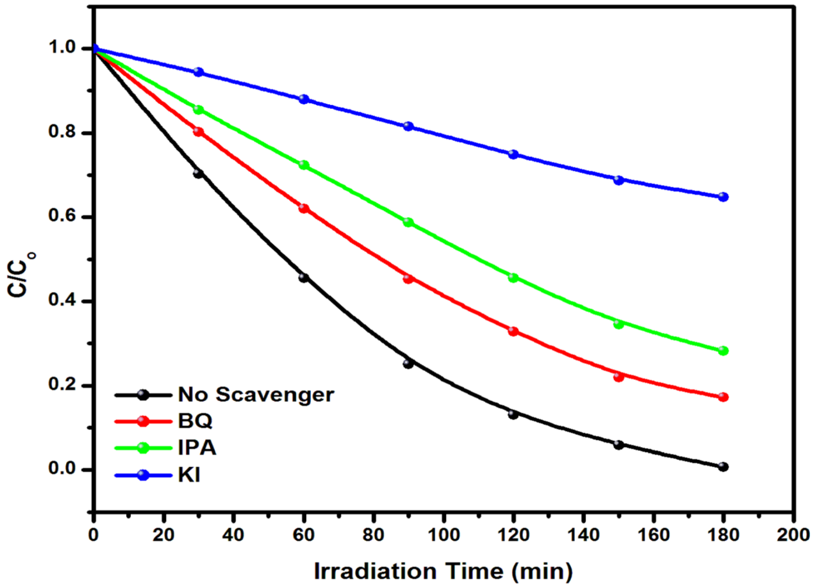

Figure 9. Time vs concentration plot of three different quenching agents, IPA, KI, and BQ quenchers, for the catalytic properties of 25% Tb/$Bi_4V_2O_{11}$.

The complex plane plots of impedance for the investigated Tb/$Bi_4V_2O_{11}$ samples show a behavior typical for the oxygen-conducting $Bi_4V_2O_{11}$ nanoparticles for all compositions at the same temperature. It is interesting to note that the variation of single substitution composition results in various impedance regions. Conductivity is dramatically enhanced upon doping $Bi_4V_2O_{11}$ with 15 and 20% Tb /$Bi_4V_2O_{11}$, and the highest conductivity is observed in 25% Tb /$Bi_4V_2O_{11}$. The impedance of the electrode−electrolyte interface is clearly represented by the inclined spikes appearing at very low frequencies.[25,56−58] 25% Tb/$Bi_4V_2O_{11}$ exhibited a single semicircle resulting from overlapping of both the grain and grain boundary contributions usually encountered at lower temperatures with no prominent electrode−electrolyte spike.[24]

Table 2 presents the values of equivalent circuit parameters for grain contribution estimated from the impedance plane plots for a temperature of 300 °C at different concentrations (x = 0, 15, 20, and 25%). It can also be noticed that the reduction in R_g values increases with increasing concentration of Tb^{3+}. Moreover, the values of C_g are less at lower Tb^{3+} concentration, which suggests that the permittivity increases with the accumulation of charge carriers at the grain. The highest values of capacitance C_g for $x = 25\%$ is found to be 1.52×10^{-5} at 300 °C, suggesting more polarizability of the sample at this temperature and composition. Hence, the total electrical permittivity of the sample is mainly attributed to the increased charge accumulation in the grain.[28] The ionic conductivity is calculated and found to be the highest for 25% Tb/$Bi_4V_2O_{11}$ (15.92 S cm^{-1}).

2.7. Photocatalytic Reduction of Cadmium Ions (Cd II). A photocatalytic reductive elimination of heavy metals (Cd II ions) from aqueous solution under visible light illumination was investigated for the prepared nanomaterial. Photocatalytic reductive activity is shown generally by the charging carrier. The synthesized nanoparticles have stronger visible-light absorption, higher adsorption of contaminants, and greater exposure to more active sites that leads to higher activity. The band gap of the synthesized nanoparticles was also calculated as shown in Figure 8b. The band gaps were calculated and found to be equal to 2.0 and 1.8 eV for $Bi_4V_2O_{11}$ and 25% Tb/$Bi_4V_2O_{11}$, respectively. Tb^{3+} ion substitution in the $Bi_4V_2O_{11}$ host lattice shows a red shift. The position of the UV band shifts toward higher wavelengths. Figure 8a shows the photocatalytic reduction (at pH 9) of Cd (II) in the presence of 25% Tb/$Bi_4V_2O_{11}$ under UV−visible light illumination. The inset of Figure 8a shows the influence of pH on the photoreduction of Cd (II). The amounts of Cd (II) reduced to Cd (0) at pH values of 4, 5, 6, and 9 are 54, 66, 74, and 79%, respectively, for 25% Tb/$Bi_4V_2O_{11}$. It can be observed that the highest reduction is seen at pH 9. Moreover, upon increasing the pH, the photoreductive capability increases because of the tendency of hydrolysis of Cd (II). At a pH higher than 9, cadmium ions start to precipitate out as $Cd(OH)_2$ and the photoreduction decreases.

Figure 8a shows that Cd (II) reduction starts after exposure to light and the maximum absorption steadily decreases with the irradiation time. Figure 8a exhibits the change in the absorbance of Cd (II) with respect to the irradiation time, indicating 85% reduction after 180 min. It can be clearly seen in Figure 8c that with 25% Tb/$Bi_4V_2O_{11}$ nanoparticles compared to other doping materials and $Bi_4V_2O_{11}$, the reduction of Cd (II) was exceptional and more rapid.[15,21,23,59] The kinetic analysis for heavy metal reduction is crucial for determining the utility and feasibility of toxic water bodies.

The kinetic reaction rate depends only on Cd (II) levels in the present study since the concentration of water is constant as it is present in excess during the reaction cycle.[60] The reduction rate for Cd (II) can be well fitted using the following equation.

$$\ln C/C_o = -Kt \tag{2}$$

where C_o is the initial concentration and C is the concentration at time t. Figure 8d shows the plot between ln C/C_o versus irradiation time. From nonlinear fitting curve,[61] it is concluded that the kinetic rate (K) of 25% Tb/$Bi_4V_2O_{11}$ is 0.0106 ± 0.01 min^{-1}. The kinetic results show that 25% Tb/$Bi_4V_2O_{11}$ is

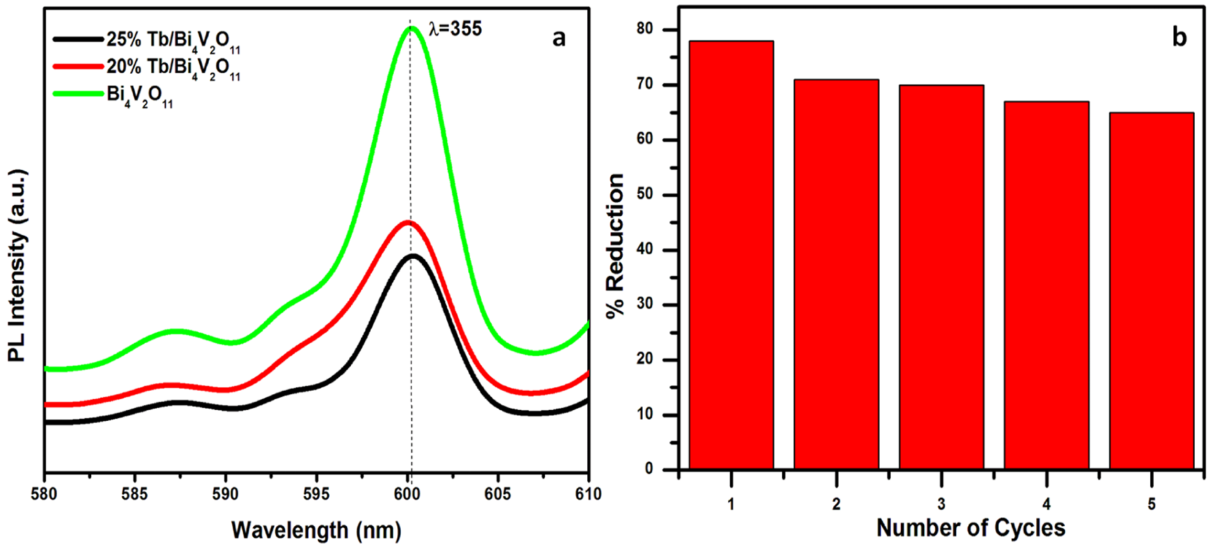

Figure 10. (a) Time vs concentration plot of three different quenching agents, IPA, KI, and BQ quenchers, for the catalytic properties of 25% Tb/$Bi_4V_2O_{11}$ and (b) plot of the reduction rate of Cd as a function of the number of cycles. The photostability of the 25% Tb/$Bi_4V_2O_{11}$ sample was tested in photoreduction of Cd under identical reaction conditions. Less than 7% reduction in the photocatalytic activity was observed after five consecutive cycles.

efficient for degradation of hazardous pollutants such as Cd 4(II).

In 25% Tb/$Bi_4V_2O_{11}$, the radical and hole trapping experiments were investigated. Three different quenching agents, namely, isopropanol (IPA, 10 mM $^{\cdot}$OH quencher), potassium iodide (KI, 10 mM, h^+ and $^{\bullet}$OH quencher), and benzoquinone (BQ, 1 mM $^{\bullet}O_2^-$ quencher) were used. It could be seen in Figure 10 that the catalytic properties of 25% Tb/$Bi_4V_2O_{11}$ were partially affected by IPA, indicating that during the photocatalytic process, the hydroxyl radical ($^{\bullet}$OH) is one of the key radicals. The photoreductive activity decreased after adding KI, indicating that during the reduction of Cd (II), h^+ not only directly oxidizes to degrade pollutants but also generates $^{\bullet}$OH. The effect of BQ on the photoreduction action suggests that the superoxide radical plays a vital role in this whole process. The energies of valence band and conduction band (CB) can be calculated according to the equation

$$E_{\mathrm{VB}} = \chi - E_{\mathrm{e}} + 0.5E_{\mathrm{g}} \tag{3}$$

$$E_{\mathrm{CB}} = E_{\mathrm{VB}} - E_{\mathrm{g}} \tag{4}$$

where χ is the electronegativity of the semiconductors (for $Bi_4V_2O_{11}$, χ is 6.18), E_e is the energy of free electrons (4.5 eV), and E_g is the semiconductor band gap. The VB and CB potentials of $Bi_4V_2O_{11}$ were calculated to be 2.68 and 0.68 eV, respectively. It is worth noting that the quenching experiment results (Figure 9) showed that the superoxide radical ($^{\bullet}O_2^-$) also occupies a significant position in the photoreductive procedure, which means that 25% Tb/$Bi_4V_2O_{11}$ can efficiently use the electrons generated by the photoelectricity to generate the $^{\bullet}O_2^-$ radical.

2.8. Photoluminescence, Photostability, and Reusability of the 25% Tb/$Bi_4V_2O_{11}$ Nanocatalyst. The recombination of photogenerated electron−hole pairs is an essential parameter for evaluating a catalyst's photoreductive efficiency. The separation efficiency of photogenerated electron−hole pairs was investigated using photoluminescence (PL) spectroscopy. In this case, a high fluorescence intensity generally corresponds to the significant recombination of electron−hole pairs. Therefore, as shown in Figure 10a, the main emission peak for $Bi_4V_2O_{11}$ is centered at approximately 600 nm. The broad and low-intensity peak for 25% Tb/$Bi_4V_2O_{11}$ arising from the oxygen vacancies in its lattice extremely quenches the $Bi_4V_2O_{11}$ emission at the same position. The prominent peak located at 600 nm is consistent, but peak intensities changed dramatically. This transition may be attributed to defects corresponding to the Tb^{3+} and V^{5+} content, which affect particle sizes and defect levels, but the PL emission is primarily dependent on the Tb^{3+} content since its inclusion causes changes in defects or material disorder.[22] More oxygen vacancies are formed as the Tb^{3+} content rises, affecting the properties of solid electrolytes. This effect has been observed previously in XRD and UV−vis absorption experiments. Furthermore, as the Tb^{3+} content increases, the particle size decreases, slowing the recombination rate of electrons in the $Bi_4V_2O_{11}$ valence band (VB) and Tb conduction bands (CB) with holes in the O 2p VB. Because of the effective charge carrier isolation and lower recombination rate, lower PL strength generally leads to higher conductivity and higher oxygen vacancy concentration. This result indicates that as compared to $Bi_4V_2O_{11}$, the 25% Tb/$Bi_4V_2O_{11}$ nanomaterial has a lower electron−hole recombination rate. The photostability of the synthesized 25% Tb/$Bi_4V_2O_{11}$ nanoparticles was checked by reusing the photocatalyst up to 5 times. It is concluded that (Figure 10b) a minor reduction is observed in the efficiency after five consecutive cycles. This specifies that 25% Tb/$Bi_4V_2O_{11}$ has an excellent photoreductive ability during irradiation.

3. CONCLUSIONS

In this study, $Bi_4V_2O_{11}$ (x = 0, 15, 20, and 25%) were synthesized by the sol−gel method. We have shown the presence of the monoclinic (α) phase in the parent compound and tetragonal (γ) phase in the 25% Tb/$Bi_4V_2O_{11}$ through detailed PXRD and Raman studies. The monoclinic α-phase dominates in $Bi_4V_2O_{11}$ and 15% Tb/$Bi_4V_2O_{11}$. Optimal orthorhombic β-phase formation takes place for 20% Tb/$Bi_4V_2O_{11}$ at room temperature. From SEM and PXRD analysis, it was revealed that the synthesized nanoparticles obtained were in the range between 25 and 35 nm. The ionic conductivity was calculated and found to be the highest for 25% $Tb/Bi_4V_2O_{11}$ in the order of 15.92 S cm^{-1}. The synthesized nanoparticles (25% $Tb/Bi_4V_2O_{11}$) show high photocatalytic reduction of Cd (II) under visible light irradiation. The photocatalytic reduction of Cd (II) by the $Bi_4V_2O_{11}$ and $Tb/Bi_4V_2O_{11}$ nanomaterial can be attributed to their physical properties such as nanosized particles and large surface area. The kinetic results show that 25% $Tb/Bi_4V_2O_{11}$ is efficient for degradation of hazardous pollutants such as Cd (II).

4. EXPERIMENTAL SECTION

4.1. Synthesis of $Tb/Bi_4V_2O_{11}$. All reagents used were of analytical grade and used as received without any further purification. The doped samples were synthesized by the sol−gel method.

The required amounts of $Bi(NO_3)_3{\cdot}5H_2O$, V_2O_5, and $Tb(NO_3)_3{\cdot}6H_2O$ were weighed according to the stoichiometric formula $BiTb_xV_{2-x}O_{11+\delta}$ ($0 \leq x \leq 25$), where x is in atomic % (abbreviated as xTb/$Bi_4V_2O_{11}$), and were dissolved in distilled water under constant stirring and heating at 80 °C to obtain a yellow-colored solution. To this solution, citric acid was added, and pH was maintained at 7 by adding ammonia solution. Ethylene glycol was added (which prevents the agglomeration of particles) until the solution became homogeneous. Stirring and heating of the solution continued for 12 h. The resin was formed after evaporation and polymerization. This resin was heated at 400 °C in air. After subsequent heat treatment, the final powder was obtained. After complete calcination, pellets of $Tb/Bi_4V_2O_{11}$ were prepared similarly as discussed earlier.[3,22]

4.2. Photocatalytic Reduction of Cadmium (II). Double distilled water was used for making 50 mL of $CdCl_2$ solution (20 ppm). All investigations were carried out by circulation of cold water in the outer wall under correct cooling conditions to prevent thermal reactions. In a typical process, 180 mg (1 g/L) of the synthesized catalyst was oscillated at a rotation speed of 180 rpm at room temperature. The solution was quickly taken out for filtration at a predetermined time to determine the mass concentration of Cd (II) in the solution. As mentioned by Hossein et al., on increasing pH from 4 to 7, the percent of photoreduction decreased.[2] It is suggested that the photoreduction of the metallic cation is significantly dependent on their tendency toward the hydrolysis reaction.[1,62,63]

$$\text{Metal ion}^{2+}(\text{aq}) + n(\text{water}) \rightarrow \text{metal}(\text{OH})^{2-n} + n\text{H}^+ \tag{5}$$

According to the above eq 5, metal hydroxide dispersion is effectively done if the pH and the stability of the metal hydroxide of the solution are proper. If we take into account the cadmium ion, cadmium hydroxide precipitates out at pH 9 effectively. According to Hossain et al., the photocatalyst becomes unstable if the metallic ions are reduced. On the basis of the above observations, the reaction is carried out at different pH values from 4 to 9 in order to find out the pH at which maximum reduction takes place.

A UV−vis spectrophotometer was used to analyze the photocatalytic reduction efficiency. In order to monitor the pollutant degradation, the following formula was used for the maximum absorption rate of Cd (II) at 430 nm.

$$\eta = C_o - C/C_o \tag{6}$$

where C_o is the initial concentration and C is the concentration at time T of the pollutant. The catalyst used for photoreduction in the centrifuge was used in the whole experiment and further washed with distilled water and reused for testing the stability and reusability.

4.3. Characterizations. The synthesized samples of various concentrations of $Tb/Bi_4V_2O_{11}$ were characterized at room temperature by X-ray powder diffraction using a Philips PW 1050/30 X-ray diffractometer with CuKα radiation (λ = 1.54060 Å). The unit cell parameters were calculated with the help of the X'Pert Highscore Plus software program.

The surface microstructures of the nanoparticles were studied through scanning electron microscopy (SEM) (JEOL-2100) and high-resolution transmission electron microscopy (HR-TEM) analyses. The chemical composition and sample purity were studied by energy-dispersive analysis (EDAX) results. The conduction properties were analyzed by using AC impedance spectroscopy with a Wayne Kerr 4100 LCR meter operated in the frequency range from 1 Hz to 1 MHz operated with an AC signal of ∼50 mV. For AC impedance measurements, all the sintered pellets were made conductive, as discussed in earlier research.[3,24,64]

AUTHOR INFORMATION

Corresponding Author

Saba Beg − *Physical Chemistry Lab Department of Chemistry, Aligarh Muslim University, Aligarh 202002, India;* orcid.org/0000-0002-7781-1747; Email: profsababeg@gmail.com

Authors

Faria K. Naqvi − *Physical Chemistry Lab Department of Chemistry, Aligarh Muslim University, Aligarh 202002, India*

Kaseed Anwar − *Physical Chemistry Lab Department of Chemistry, Aligarh Muslim University, Aligarh 202002, India*

Complete contact information is available at:
https://pubs.acs.org/10.1021/acsomega.1c04400

Notes

The authors declare no competing financial interest.

ACKNOWLEDGMENTS

F.K.N. (file no. 09/112(0612)/2019-EMR-I) and K.A. (file no. 09/112(0652)/2019-EMR-I) are grateful to the CSIR, New Delhi, India, for granting the Senior Research Fellowship (SRF) and Junior Research Fellowship (JRF), respectively. They would also like to express their sincere gratitude to the Chairperson, Department of Chemistry, Aligarh Muslim University, Aligarh, for providing requisite research facilities. They also want to acknowledge the ECOR Foundation for their enormous work to protect the nature.

REFERENCES

(1) Xue, Z.; et al. Adsorption of Cd (II) in water by mesoporous ceramic functional nanomaterials. *R. Soc. Open Sci.* **2019**, *6*, 182195.

(2) Salmanvandi, H.; Rezaei, P.; Tamsilian, Y. Photoreduction and Removal of Cadmium Ions over Bentonite Clay-Supported Zinc Oxide Microcubes in an Aqueous Solution. *ACS Omega* **2020**, *5*, 13176−13184.

(3) Naqvi, F. K.; Faraz, M.; Beg, S.; Khare, N. Synthesis and Phase Transformation Studies of Dysprosium-Doped Bi4V2O11 Nanoparticles and Their Application in Visible Light Photocatalytic Degradation of Tetracycline Drug. *ACS Omega* **2018**, *3*, 11300−11306.

(4) Ullah, M.; Haque, M. E. Spectrophotometric Determination of Toxic Elements (Cadmium) in Aqueous Media. *J. Chem. Eng.* **2011**, *25*, 1−25.

(5) Ghafoor, S.; Hussain, S. Z.; Waseem, S.; Arshad, S. N. Photoreduction of heavy metal ions and photo-disinfection of pathogenic bacteria under simulated solar light using photosensitized TiO2 nanofibers. *RSC Adv.* **2018**, *8*, 20354−20362.

(6) Huang, Y.; et al. Heavy metal pollution and health risk assessment of agricultural soils in a typical peri-urban area in southeast China. *J. Environ. Manage.* **2018**, *207*, 159−168.

(7) Ali, M. M.; Ali, M. L.; Islam, M. S.; Rahman, M. Z. Preliminary assessment of heavy metals in water and sediment of Karnaphuli River, Bangladesh. *Environ. Nanotechnol. Monit. Manag.* **2016**, *5*, 27−35.

(8) Warad, I.; et al. Structural studies on Cd(II) complexes incorporating di-2-pyridyl ligand and the X-ray crystal structure of the chloroform solvated DPMNPH/CdI2 complex. *Inorg. Chem. Commun.* **2014**, *43*, 155−161.

(9) Al-Resayes, S. I.; Shakir, M.; Shahid, N.; Azam, M.; Khan, A. U. Synthesis, spectroscopic characterization and in vitro antimicrobial studies of Schiff base ligand, H2L derived from glyoxalic acid and 1,8-diaminonaphthalene and its Co(II), Ni(II), Cu(II) and Zn(II) complexes. *Arabian J. Chem.* **2016**, *9*, 335−343.

(10) Ihsanullah.; et al. Heavy metal removal from aqueous solution by advanced carbon nanotubes: Critical review of adsorption applications. *Sep. Purif. Technol.* **2016**, *157*, 141−161.

(11) Vilela, D.; Parmar, J.; Zeng, Y.; Zhao, Y.; Sánchez, S. Graphene-Based Microbots for Toxic Heavy Metal Removal and Recovery from Water. *Nano Lett.* **2016**, *16*, 2860−2866.

(12) Sangeetha, K.; Vidhya, G.; Vasugi, G.; Girija, E. K. Lead and cadmium removal from single and binary metal ion solution by novel hydroxyapatite/alginate/gelatin nanocomposites. *J. Environ. Chem. Eng.* **2018**, *6*, 1118−1126.

(13) Genchi, G.; Maria, S. S.; Graziantono, L.; Carocci, A.; Alessia, C. The Effects of CadmiumToxicity. *Int. J. Environ. Res. Public Health* **2020**, *17*, 3782.

(14) Azam, M.; et al. Cu(II) salen complex with propylene linkage: An efficient catalyst in the formation of C X bonds (X = N, O, S) and biological investigations. *J. Mol. Struct.* **2017**, *1130*, 122−127.

(15) Sane, P.; Chaudhari, S.; Nemade, P.; Sontakke, S. Photocatalytic reduction of chromium (VI) using combustion synthesized TiO2. *J. Environ. Chem. Eng.* **2018**, *6*, 68−73.

(16) Nu, V.; Nguyen, H.; Amal, R.; Beydoun, D. E ect of formate and methanol on photoreduction /removal of toxic cadmium ions using TiO 2 semiconductor as photocatalyst. *Chem. Eng. Sci.* **2003**, *58*, 4429−4439.

(17) Mishra, T.; Hait, J.; Aman, N.; Jana, R. K.; Chakravarty, S. Effect of UV and visible light on photocatalytic reduction of lead and cadmium over titania based binary oxide materials. *J. Colloid Interface Sci.* **2007**, *316*, 80−84.

(18) Li, S.; et al. TiO2@Pt@CeO2 nanocomposite as a bifunctional catalyst for enhancing photo-reduction of Cr (VI) and photo-oxidation of benzyl alcohol. *J. Hazard. Mater.* **2018**, *346*, 52−61.

(19) Xu, C.; Cui, R.; Fu, L.; Lin, B. Recyclable and heat-healable epoxidized natural rubber/bentonite composites. *Compos. Sci. Technol.* **2018**, *167*, 421.

(20) Zhou, G.; Luo, J.; Liu, C.; Chu, L.; Crittenden, J. Efficient heavy metal removal from industrial melting effluent using fixed-bed process based on porous hydrogel adsorbents. *Water Res.* **2018**, *131*, 246−254.

(21) Li, Y.; et al. Carbon dots-TiO2 nanosheets composites for photoreduction of Cr(VI) under sunlight illumination: favorable role of carbon dots. *Appl. Catal., B* **2018**, *224*, 508.

(22) Naqvi, F. K.; Beg, S. Synthesis of visible light active copper, iron co-doped BiVO4 photocatalyst for the degradation of phenol. *React. Kinet. Mech. Catal.* **2020**, *131*, 409.

(23) Zheng, F.; Lin, X.; Yu, H.; Li, S.; Huang, X. Visible-light photoreduction, adsorption, matrix conversion and membrane separation for ultrasensitive chromium determination in natural water by X-ray fluorescence. *Sens. Actuators, B* **2016**, *226*, 500−505.

(24) Beg, S.; Naqvi, F. K.; Al-areqi, N. A. S. Study on electrical conductivity and phase transition in singly doped BIPBVOX (Bi2V1−xPbxO5.5−x/2) solid electrolyte. *Phase Transitions* **2014**, *87*, 1225−1236.

(25) Lazure, S. Composition dependence of oxide anion conduction in the BIMEVOX family. *Solid State Ionics* **1996**, *90*, 117−123.

(26) Beg, S.; Hafeez, S.; Al-Areqi, N. a. S. Layered Bi4BaxV2-xO11-(3x/2)-δ perovskite oxide as solid electrolyte for intermediate temperature solid oxide fuel cells. *Phys. B* **2010**, *405*, 4370−4376.

(27) Beg, S.; Al-Alas, A.; Al-Areqi, N. A. S. Layered Aurivillius compound: Synthesis, characterization and electrical properties. *J. Alloys Compd.* **2010**, *504*, 413−419.

(28) Al-Alas, A.; Beg, S.; A.S.Al-Areqi, N.; Hafeez, S. Influence of microwave-assisted calcination on structural properties and oxide-ion performance of layered-perovskite γ-BIMNVOX solid electrolyte synthesized by ethylene glycol-citrate sol-gel route. *J. Eur. Ceram. Soc.* **2013**, *33*, 2111−2117.

(29) Singh, B.; Ghosh, S.; Aich, S.; Roy, B. Low temperature solid oxide electrolytes (LT-SOE): A review. *Power Sources* **2017**, *339*, 103−135.

(30) Al-Alas, A.; Beg, S.; Al-Areqi, N. A. S. Investigation of phase stability and oxide ion performance in new perovskite-type bismuth vanadate. *Mater. Chem. Phys.* **2012**, *136*, 15−20.

(31) Beg, S.; Al-Areqi, N. A. S. Structural and electrical study of CeIV-substituted bismuth vanadate. *J. Phys. Chem. Solids* **2009**, *70*, 1000−1007.

(32) Beg, S.; Varshney, P.; Sarita. Study of electrical conductivity changes and phase transitions in TiO2 doped ZrO2. *J. Mater. Sci.* **2007**, *42*, 6274−6278.

(33) Zhu, J. X.; et al. Grain boundary conductivity of high purity neodymium-doped ceria nanosystem with and without the doping of molybdenum oxide. *J. Power Sources* **2007**, *174*, 114−123.

(34) Beg, S.; Hafeez, S.; Al-Areqi, N. a. S. Study of phase stabilization and oxide-ion conductivity in BICUMGVOX solid electrolyte. *Solid State Ionics* **2014**, *261*, 125−130.

(35) Kant, R.; Singh, K.; Pandey, O. P. Ionic conductivity and structural properties of MnO-doped Bi4V2O11 system. *Ionics* **2009**, *15*, 567.

(36) Ramos-Alvarez, P.; et al. Ceria-based electrolytes with high surface area and improved conductivity for intermediate temperature solid oxide fuel cells. *J. Mater. Sci.* **2017**, *52*, 519−532.

(37) Mercier, F.; Alliot, C.; Bion, L.; Thromat, N.; Toulhoat, P. XPS study of Eu(III) coordination compounds: Core levels binding energies in solid mixed-oxo-compounds EumXxOy. *J. Electron Spectrosc. Relat. Phenom.* **2006**, *150*, 21−26.

(38) Lin, X.; et al. Graphitic carbon nitride quantum dots and nitrogen-doped carbon quantum dots co-decorated with BiVO4 microspheres: A ternary heterostructure photocatalyst for water purification. *Sep. Purif. Technol.* **2019**, *226*, 117−127.

(39) Zhang, Y.; et al. Facile synthesis of V4+self-doped, [010] oriented BiVO4nanorods with highly efficient visible light-induced photocatalytic activity. *Phys. Chem. Chem. Phys.* **2014**, *16*, 24519−24526.

(40) Li, D.; Wang, W.; Jiang, D.; Zheng, Y.; Li, X. Surfactant-free hydrothermal fabrication of monoclinic BiVO4 photocatalyst with oxygen vacancies by copper doping. *RSC Adv.* **2014**, *5*, 14374.

(41) Walsh, A.; Yan, Y.; Huda, M. N.; Al-Jassim, M. M.; Wei, S.-H. Band Edge Electronic Structure of BiVO4: Elucidating the Role of the Bi s and V d Orbitals. *Chem. Mater.* **2009**, *21*, 547−551.

(42) Merupo, V. I.; Velumani, S.; Structural , morphological and optical properties of sol-gel prepared Cu doped BiVO 4 powders.

2015 12th International Conference on Electrical Engineering, Computing Science and Automatic Control (CCE); IEEE, 2015; pp 1−5.

(43) Zarrin, H.; et al. Quaternized Graphene Oxide Nanocomposites as Fast Hydroxide Conductors. *ACS nano* **2015**, *9*, 2028−2037.

(44) Liu, H.; et al. Incorporation of Ammonia Borane Groups in the Lithium Borohydride Structure Enables Ultrafast Lithium Ion Conductivity at Room Temperature for Solid-State Batteries. *Chem. Mater.* **2020**, *32*, 671−678.

(45) Us, S.; et al. Sımple Method For The Determınatıon of Band Gap of a Nanopowdered Sample Usıng Kubelka Munk Theory. *J. Niger. Assoc. Math. Phys.* **2016**, *35*, 241−246.

(46) Merupo, V. I.; Velumani, S. Structural and Optical properties of Molybdenum doped Bismuth vanadate powders.*2014 11th International Conference on Electrical Engineering, Computing Science and Automatic Control (CCE)*; IEEE 2014.

(47) Luo, Y.; et al. Applied Surface Science Structural transformation of Sm3+ doped BiVO4 with high photocatalytic activity under simulated sun-light. *Appl. Surf. Sci.* **2015**, *324*, 505−511.

(48) Bacewicz, R.; Kurek, P. Raman scattering in BIMEVOX (ME 5 Mg , Ni , Cu , Zn) single crystals. *Solid State Ionics* **2000**, *127*, 151−156.

(49) Hardcastle, F. D.; Wachs, I. E. Vanadium (V) Investigation Environments in Bismuth Vanadates : A Structural Using Raman Spectroscopy and Solid State 51 V NMR. *J. Solid State Chem.* **1991**, *90*, 194−210.

(50) Zoellner, B.; et al. CuNb1-xTaxO3 (x </=0.25) solid solutions: impact of Ta(V) substitution and Cu(I) deficiency on their structure, photocatalytic, and photoelectrochemical properties. *Mater. Chem. A* **2016**, *4*, 3115−3126.

(51) Faraz, M.; Naqvi, F. K.; Shakir, M.; Khare, N. Synthesis of samarium-doped zinc oxide nanoparticles with improved photocatalytic performance and recyclability under visible light irradiation. *New J. Chem.* **2018**, *42*, 2295−2305.

(52) Vaidhyanathan, B.; Balaji, K.; Rao, K. J. Microwave-Assisted Solid-State Synthesis of Oxide Ion Conducting Stabilized Bismuth Vanadate Phases. *Chem. Mater.* **1998**, *10*, 3400−3404.

(53) Breitkopf, C. *Impedance Spectroscopy Old Technique—New Applications*; Fritz Haber Institute, 2012.

(54) Losilla, E. R.; Martı, M. C.; Sheptyakov, D. V.; Aranda, M. A. G. High Oxide Ion Conductivity in Al-Doped Germanium Oxyapatite. *Chem. Mater.* **2005**, *17*, 596−600.

(55) Kurzweil, P. ac Impedance Spectroscopy − A Powerful Tool For The Characterization Of Materials And Electrochemical Power Sources. *Proceedings OF 14th International Seminar On double layer Capacitors*, 2004.

(56) Al-Areqi, N. a. S.; Beg, S.; Al-Alas, A. Study on phase stability and oxide ion conductivity in the BIAGVOX system. *J. Phys. Chem. Solids* **2012**, *73*, 730−734.

(57) Nguyen, T. L.; Dokiya, M. Electrical conductivity, thermal expansion and reaction of (La, Sr)(Ga, Mg)O and (La, Sr)AlO system. *Solid State Ionics* **2000**, *132*, 217−226.

(58) Beg, S.; Haneef, S.; Al-Areqi, N. a S. Study of phase transition of TiO2-CaO system. *Ionics* **2010**, *16*, 239−244.

(59) Zhang, Y.; Xu, M.; Li, H.; Ge, H.; Bian, Z. *Appl. Catal., B* **2018**, *226*, 213.

(60) Raza, W.; Faraz, M. Novel g-C3N4/Fe-ZnO/RGO nanocomposites with boosting visible light photocatalytic activity for MB, Cr (VI) and outstanding catalytic activity towards para-nitrophenol reduction. *Nanotechnology* **2020**, *31*, 325603.

(61) Gabor, L. ScienceDirect Facts and alternative facts in chemical kinetics : remarks about the kinetic use of activities , termolecular processes , and linearization techniques. *Curr. Opin. Chem. Eng.* **2018**, *21*, 76−83.

(62) Etacheri, V.; Di Valentin, C.; Schneider, J.; Bahnemann, D.; Pillai, S. C. Visible-light activation of TiO2 photocatalysts: Advances in theory and experiments. *J. Photochem. Photobiol. C Photochem. Rev.* **2015**, *25*, 1−29.

(63) Karim, M. R.; et al. Composite nanofibers membranes of poly(vinyl alcohol)/chitosan for selective lead(II) and cadmium(II) ions removal from wastewater. *Ecotoxicol. Environ. Saf.* **2019**, *169*, 479−486.

(64) Naqvi, F. K.; Beg, S.; Al-areqi, N. A. S. Structural and Cyclic Volta metric Investigations on BIPBVOX Solid Electrolyte Synthesized by Ethylene glycol − Citric Acid Sol − Gel Route. *AIP Conference Proceedings*; AIP Publishing LLC, 2015; Vol. *7*, p 10.